Journal of Biological Engineering

RESEARCH

Open Access

Amplification-free CRISPR/Cas13a-based electrochemical biosensor for the detection of circulating tumor RNA using RNA-3Ag$^+$ probes on Au porous-lattice nanoelectrode

Yu-Rim Lee[1†], Myeong-Jun Lee[2†], Sang-Nam Lee[2,3*] and Jeong-Woo Choi[1,2*]

Abstract

Circulating tumor RNA (ctRNA) is a sensitive biomarker for early cancer diagnosis, offering real-time gene expression profiles and tumor-specific signatures missed by circulating tumor DNA. Despite its potential, a simple, rapid, and sensitive ctRNA detection sensor has not yet been developed. For the first time, we present an amplification-free electrochemical biosensor for ctRNA detection by integrating the CRISPR/Cas13a system with a silver ion (Ag^+)-mediated RNA probe and an Au porous-lattice nanoelectrode (APLNE). A three-cytosine-cytosine (C–C) mismatched RNA duplex was employed as a signal probe, allowing site-specific Ag^+ intercalation to form stable C–Ag^+–C coordination complexes (RNA-3Ag^+) that generate strong redox peaks. To further enhance performance, the APLNE, featuring a highly aligned porous gold nanostructure, was used to increase the effective surface area, improving probe immobilization and electrochemical signals. Upon target recognition, CRISPR/Cas13a cleaved the RNA-3Ag^+ probe, resulting in a significant signal reduction. This biosensor detects KRAS G12D ctRNA, a key pancreatic cancer mutation, with ultrahigh sensitivity (LOD = 0.5 fM) in just 20 min and demonstrates excellent specificity in complex biological samples. Operating without nucleic acid amplification or toxic redox reagents, this simple, cost-effective, and eco-friendly platform shows strong potential for liquid biopsy-based diagnostics and point-of-care cancer screening.

Highlights

- Amplification-free CRISPR/Cas13a-based electrochemical biosensor for ctRNA detection
- APLNE with high surface area enabling efficient signal transduction
- A redox signal enhanced by Ag^+-coordinated C–C mismatched RNA probes
- Achieve sensitive detection of KRAS G12D ctRNA with LOD = 0.5 fM within 20 mins
- Demonstrate practical applicability in human serum and cell media

[†]Yu-Rim Lee and Myeong-Jun Lee contributed equally to this work.

*Correspondence:
Sang-Nam Lee
snlee9191@hanmail.net
Jeong-Woo Choi
jwchoi@sogang.ac.kr

Full list of author information is available at the end of the article

Keywords ctRNA, KRAS G12D, CRISPR/Cas13a, Amplification-free, Electrochemical sensor

Graphical Abstract

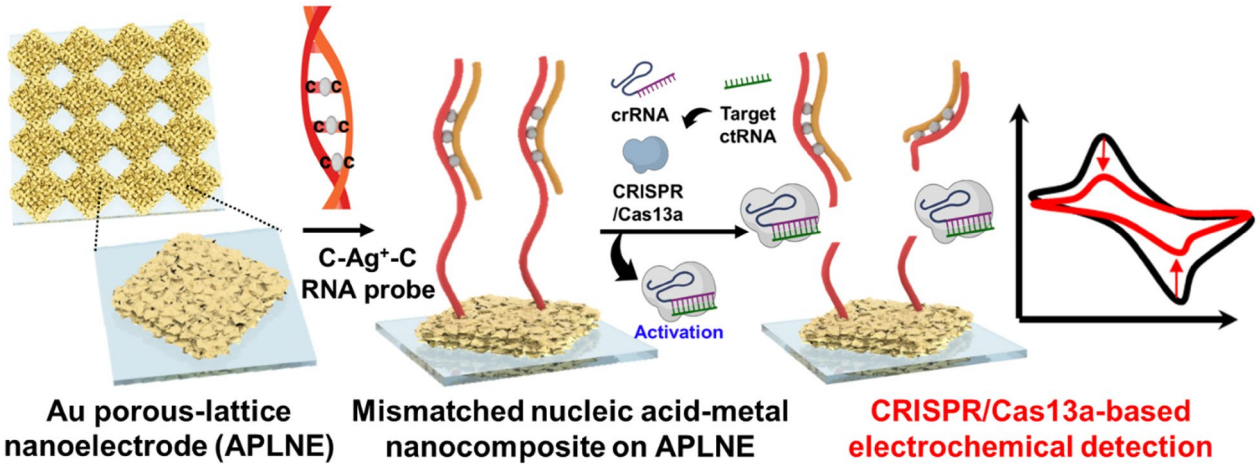

Introduction

Circulating tumor RNA (ctRNA) has become a highly informative biomarker for cancer diagnostics, as it can be obtained from a simple blood draw, offering a minimally invasive alternative to tissue biopsies [1, 2]. Unlike circulating tumor DNA (ctDNA), which mainly reflects historical genetic alterations, ctRNA provides a dynamic, real-time snapshot of tumor biology, offering valuable insights present at higher copy numbers than ctDNA in plasma, which can improve diagnostic accuracy [3–6]. These properties allow ctRNA to measure tumor status more sensitively and accurately compared to ctDNA. Among ctRNA species, oncogenic transcripts such as KRAS G12D RNA are particularly useful due to their frequent occurrence in pancreatic, colorectal, and non-small cell lung cancers and their potential utility in liquid biopsy-based molecular diagnostics [7–9]. This clinical relevance underscores ctRNA as a promising biomarker for minimally invasive cancer monitoring.

Despite this potential, translating ctRNA into practical diagnostics remains challenging. ctRNA molecules are inherently unstable, highly susceptible to RNase-mediated degradation, and present at extremely low concentrations in physiological fluids, making direct detection technically difficult. To achieve sensitive ctRNA detection, conventional molecular diagnostic techniques such as reverse transcription quantitative PCR (RT-qPCR) and next-generation sequencing (NGS) have long served as the standard approaches [10]. These methods provide high sensitivity and specificity, but their multi-step workflows, including RNA extraction, reverse transcription, and thermal cycling, are labor-intensive and time-consuming. They also require costly instrumentation and skilled personnel, limiting their applicability for rapid, decentralized, and point-of-care (POC) testing [11, 12]. With growing demand for simplified, amplification-free, and highly sensitive ctRNA detection platforms, there is a pressing need for innovative technologies that bridge the gap between clinical utility and operational feasibility.

In this context, CRISPR/Cas-based nucleic acid detection offers a powerful solution [13, 14]. Among CRISPR-associated enzymes, Cas13a is particularly valuable due to its unique collateral cleavage activity, which enables sequence-specific recognition and signal generation for RNA targets [15]. Once activated by a complementary guide RNA (crRNA)–target RNA complex, Cas13a indiscriminately cleaves nearby RNA substrates, converting target recognition directly into a measurable signal. This mechanism eliminates the need for nucleic acid amplification or complex labeling, simplifying assay workflows while maintaining high specificity and sensitivity. In recent years, integrating CRISPR detection systems with electrochemical biosensors has further enhanced their potential for rapid and portable diagnostics [16]. Electrochemical platforms offer key advantages such as miniaturization, label-free detection, low-cost operation, and compatibility with portable readout devices, making them particularly attractive for clinical use in resource-limited or POC settings [17–19].

Nevertheless, current electrochemical CRISPR sensors still face important limitations. Notably, their performance is often hindered by low probe density and inefficient surface functionalization, leading to weak electrochemical signals and limited sensitivity for ultra-low-abundance targets, particularly without nucleic acid amplification [20]. Furthermore, many reported systems continue to rely on synthetic redox reporters such as ferrocene or methylene blue, which are expensive,

environmentally hazardous, or chemically unstable [21–23]. Overcoming these barriers is essential to developing truly amplification-free, rapid, and clinically applicable ctRNA detection systems.

In this study, we present a novel CRISPR/Cas13a-based electrochemical biosensor that addresses these limitations by combining highly sensitive signal transduction with amplification-free detection in a single platform. Our system employs an Au porous-lattice nanoelectrode (APLNE) to enhance probe loading and electron transfer, together with an environmentally friendly silver ion (Ag^+)-mediated redox probe based on an RNA duplex containing three cytosine–cytosine (C–C) mismatches. In the absence of target ctRNA, Ag^+ ions specifically intercalate into the C–C mismatch sites, forming C–Ag^+–C complexes that generate a distinct electrochemical redox signal measurable by cyclic voltammetry. Upon recognition of the target RNA, Cas13a is activated and cleaves the RNA probe, disrupting the mismatch structure and preventing Ag^+ binding. This process produces a marked signal decrease, enabling highly sensitive, label-free, and amplification-free detection of ctRNA.

To demonstrate its clinical utility, we applied this biosensor to detect KRAS G12D ctRNA, a clinically relevant biomarker for pancreatic cancer, and further evaluated its performance in human serum and cell culture media to mimic complex biological conditions [24, 25]. The system exhibited high sensitivity, selectivity, and reproducibility, successfully detecting ultra-low concentrations of ctRNA without enzymatic amplification or complex sample preprocessing. These findings establish the CRISPR/Cas13a-based RNA-3Ag^+–APLNE biosensor as a promising candidate for next-generation liquid biopsy platforms and POC-compatible molecular diagnostics, addressing the unmet need for rapid, accurate, and minimally invasive ctRNA detection.

Results and discussion

Workflow of the CRISPR/Cas13a-based RNA-3Ag^+–APLNE biosensor for the detection of KRAS G12D ctRNA

The overall workflow of the CRISPR/Cas13a-based RNA-3Ag^+–APLNE biosensor for amplification-free detection of KRAS G12D ctRNA is illustrated in Fig. 1. The system integrates three key components: the APLNE as a high-sensitivity electrode, a C–C mismatched RNA duplex probe as the Ag^+-mediated signal generator, and the CRISPR/Cas13a complex for sequence-specific target recognition and signal suppression. As shown in Fig. 1A, the APLNE was fabricated by combining laser interference lithography (LIL) with a dealloying process to produce a three-dimensional porous gold nanoarchitecture. Briefly, a photoresist-coated indium tin oxide (ITO) substrate was exposed to a two-beam interference pattern, generating a periodic nanopattern without requiring a physical mask. After development, the resulting nanograting served as a template for the electrodeposition of an Au/Ag bimetallic film. Subsequent wet-chemical dealloying in concentrated nitric acid selectively removed Ag, yielding a rough, high-surface-area APLNE with enhanced electron transfer capability and abundant binding sites for RNA probe immobilization.

Following electrode fabrication, the APLNE was modified with a thiolated double-stranded RNA (dsRNA) probe containing a triple C–C mismatch region to construct the electrochemical sensing interface (Fig. 1B). After immobilization, the electrode was incubated with $AgNO_3$ solution, allowing site-specific Ag^+ intercalation into the C–C mismatches to form C–Ag^+–C coordination complexes. This stable redox-active interface produced a measurable oxidation-reduction peak in cyclic voltammetry (CV). In the absence of target RNA, the intact probe maintained strong Ag^+ binding, resulting in a high baseline electrochemical signal.

For ctRNA detection, the Cas13a–crRNA complex was introduced together with the target sample (Fig. 1C). Upon recognition of KRAS G12D ctRNA, Cas13a was activated through crRNA–target hybridization, initiating collateral cleavage of the immobilized RNA probe on the APLNE surface. Probe cleavage disrupted the C–C mismatch sites, thereby preventing Ag^+ intercalation and leading to a marked decrease in the electrochemical signal. This workflow enables direct, amplification-free, and label-free detection of ctRNA, with the entire process completed within 20 min.

APLNE fabrication and characterization

To evaluate the structural and electrochemical properties of the APLNE, a multi-step fabrication and characterization process was performed (Fig. 2). First, a dot-shaped photoresist (PR) nanopattern was fabricated on an ITO substrate using the LIL method. As shown in Fig. 2A, the corresponding SEM image confirms the highly uniform and periodic dot array formed on the ITO surface by this precise lithography approach. Next, a bimetallic Au/Ag layer was deposited onto the patterned substrate to create a lattice-like nanostructure (Fig. 2B). This intermediate electrode displayed a well-organized metallic arrangement at the nanoscale, as evident in both the SEM and schematic illustrations. Finally, selective chemical etching of Ag from the Au/Ag lattice produced the APLNE (Fig. 2C), characterized by a highly rough and porous gold architecture. The dealloying process introduced nanoscale surface roughness and porosity, resulting in a substantial increase in the electrochemically active surface area.

Atomic force microscopy (AFM) images further confirmed these morphological transitions: from the relatively flat dot-patterned PR/ITO structure (Fig. 2D-i)

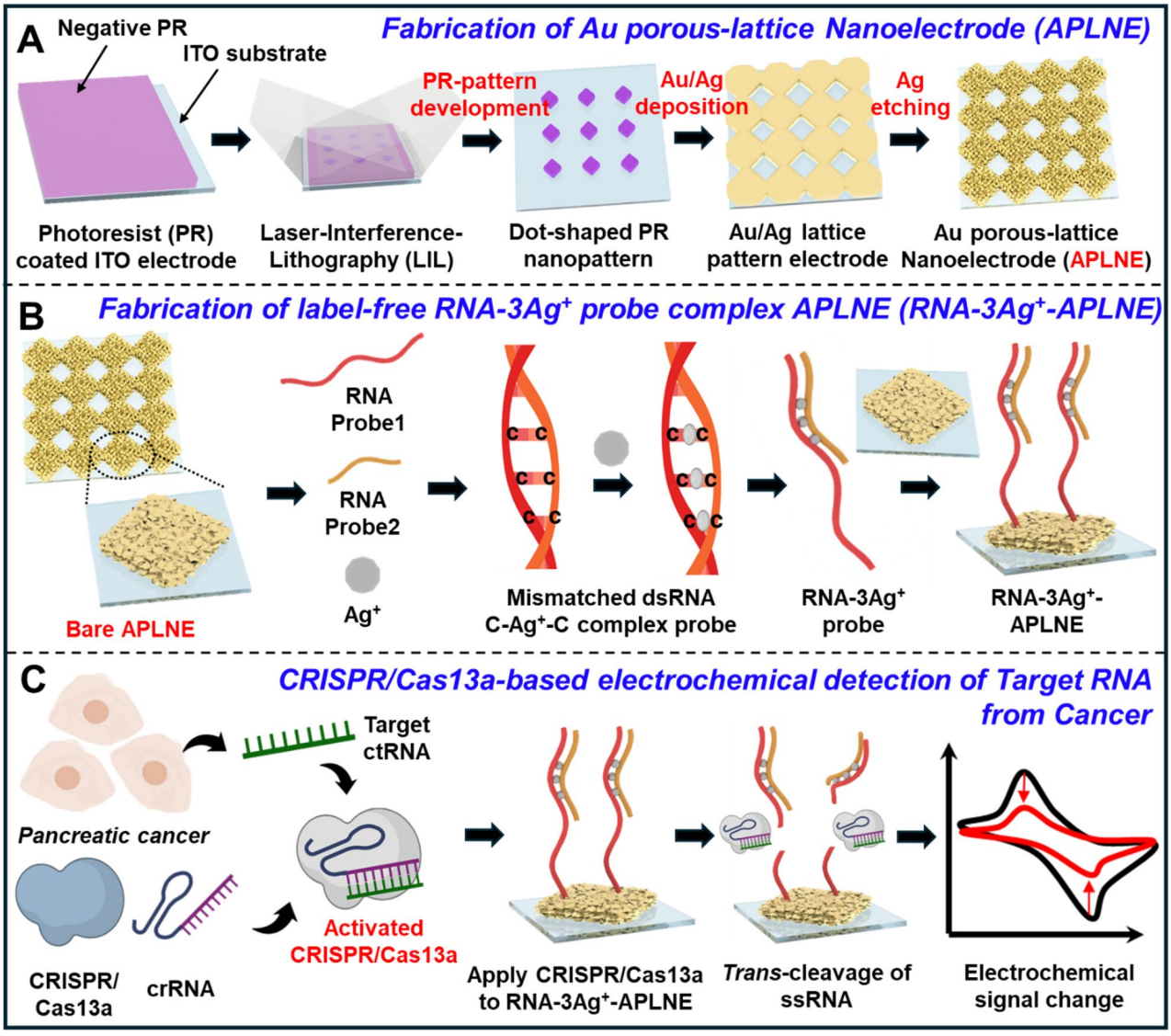

Fig. 1 Schematic illustration of the CRISPR/Cas13a-based electrochemical detection of target RNA using the RNA-3Ag$^+$–APLNE biosensor. (**A**) Fabrication process of the APLNE. (**B**) Construction of the amplification-free RNA-3Ag$^+$–APLNE biosensor using a mismatched double-stranded RNA (dsRNA) probe, Ag$^+$ ions, and APLNE. (**C**) Amplification-free CRISPR/Cas13a-based electrochemical detection of target RNA from cancer cells using the RNA-3Ag$^+$–APLNE biosensor

to the slightly roughened Au/Ag nanopattern (Fig. 2D-ii), and finally to the highly porous APLNE surface (Fig. 2D-iii).

To quantify the enhancement in electrochemical performance at each fabrication stage, CV analysis was performed using the different electrodes (ITO, Au/Ag lattice nanopattern electrode, APLNE) under identical conditions (Fig. 2E). The APLNE exhibited the highest peak current, followed by the Au/Ag nanopatterned electrode and the bare PR-patterned ITO, demonstrating a clear correlation between nanoscale surface roughness and electron transfer capability. This trend is further illustrated in a bar graph summarizing the reduction peak currents (Fig. 2F), showing that the APLNE provides a substantially enhanced electrochemical response (redox peak value = – 1,090 μA) compared to ITO (–748.7 μA) and the Au/Ag lattice nanopattern electrode (–919.6 μA), due to its expanded active surface area and improved conductivity. These results validate the effectiveness of our fabrication strategy in producing a high-performance nanoelectrode structure optimized for biosensing applications. The increased surface area not only enables higher probe immobilization but also enhances signal transduction, which is critical for achieving high sensitivity in electrochemical assays.

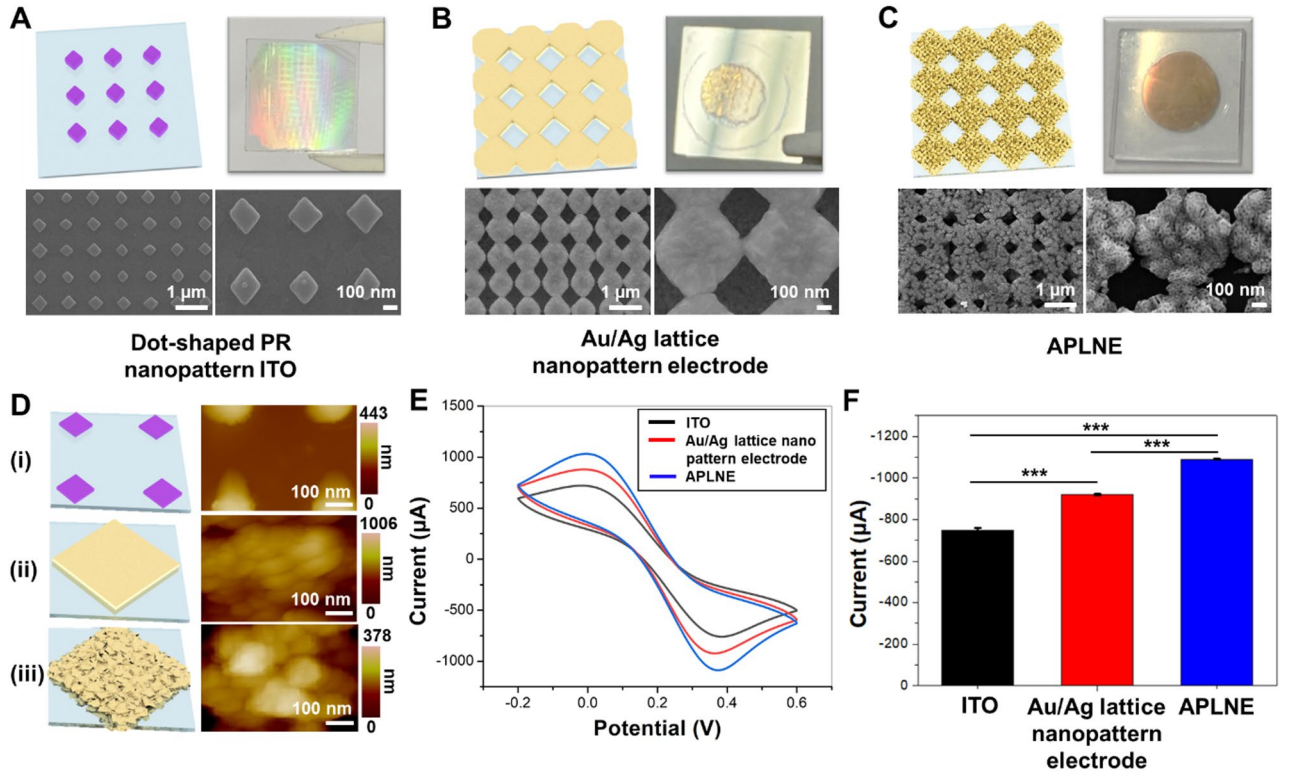

Fig. 2 Fabrication and characteristics of the APLNE. (**A**) Schematic illustration and SEM images of dot-shaped photoresist (PR) nanopatterns on an indium tin oxide (ITO) substrate generated by laser interference lithography (LIL). (**B**) Schematic and SEM images of a bimetallic Au/Ag lattice nanopattern electrode fabricated by metal deposition onto the PR-patterned ITO substrate. (**C**) Schematic and SEM images of the APLNE structure formed by selective chemical etching of Ag from the Au/Ag nanopattern, resulting in a roughened, porous gold architecture. (**D**) Atomic force microscopy (AFM) images of (i) PR nanopatterned ITO, (ii) Au/Ag lattice nanopattern electrode, and (iii) APLNE, showing progressive increases in surface roughness and porosity. (**E**) CV curves comparing the electrochemical responses of the PR nanopatterned ITO, Au/Ag nanopatterned electrode, and APLNE, demonstrating enhanced redox currents with increased surface area. (**F**) Bar graph summarizing the reduction peak currents obtained from (**E**), highlighting the superior electrochemical performance of the APLNE. All measurements were conducted in independent biological replicates ($n = 3$). Data represent mean ± SD for independent experiments. ***$p < 0.001$, Student's unpaired *t*-test

Electrochemical characterization of RNA-3Ag$^+$–APLNE

To construct the electrochemical biosensing interface, the APLNE was functionalized with a mismatched dsRNA probe, followed by C–Ag$^+$–C intercalation, forming the RNA-3Ag$^+$–APLNE complex (Fig. 3A). As illustrated in the figure, two complementary RNA strands containing a triple C–C mismatch region were immobilized on the APLNE surface. Subsequent treatment with Ag$^+$ allowed site-specific coordination into the C–C mismatches, completing the assembly of the redox-active sensing layer. Root-mean-square (RMS) roughness analysis was performed on the bare APLNE and RNA-3Ag$^+$-functionalized electrodes to evaluate surface morphology before and after probe modification (Fig. 3B). The RMS roughness value significantly decreased upon RNA-Ag$^+$ probe modification, confirming successful probe immobilization and indicating the formation of a relatively uniform molecular layer on the APLNE surface. Such reductions in surface roughness are commonly observed after biomolecular functionalization and suggest coverage by flexible organic materials such as RNA strands [26]. To validate the electrochemical activity of the immobilized RNA-Ag$^+$ probe, CV analysis was conducted under identical conditions (Fig. 3C). A clear redox signal was observed only from the RNA-3Ag$^+$-functionalized APLNE, whereas the bare APLNE and RNA-only APLNE (without Ag$^+$) showed no significant electrochemical response. These results confirm that Ag$^+$ ions specifically mediate redox-active complexation through C–C mismatches within the RNA probe, enabling electrochemical signal generation and demonstrating the successful fabrication of the redox-active sensing interface (RNA-3Ag$^+$–APLNE). This interface serves as the signal-generating layer for subsequent CRISPR/Cas13a-based detection assays.

To assess the electrochemical advantages of the APLNE substrate, we compared the performance of the RNA-Ag$^+$ probe system immobilized on two electrode surfaces: a conventional flat gold electrode (RNA-3Ag$^+$–Au) and the porous-structured APLNE (RNA-3Ag$^+$–APLNE). A schematic illustration of the comparative probe distribution is shown in Fig. 3D. Due to the significantly larger

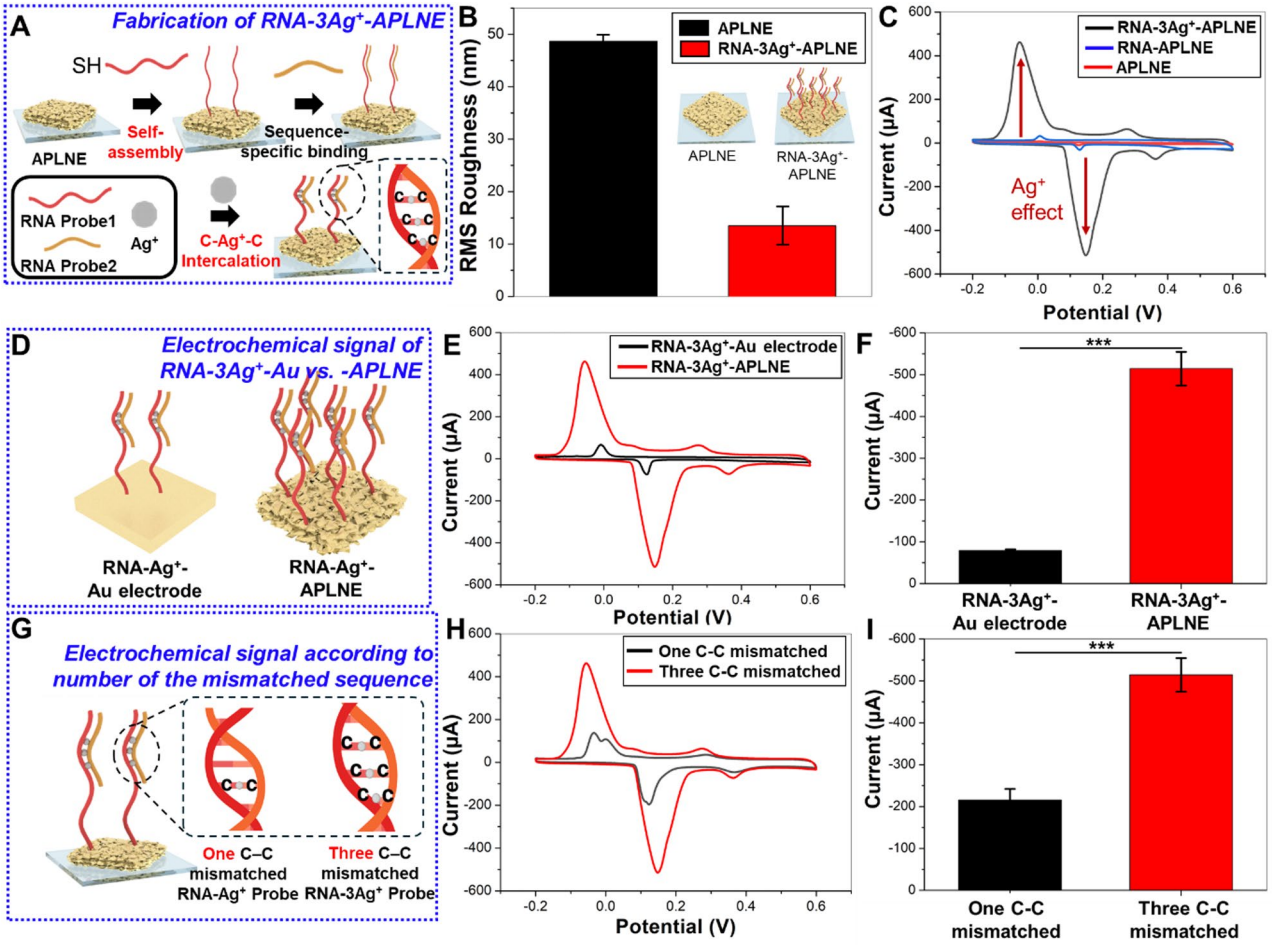

Fig. 3 Surface functionalization of the APLNE with RNA probes and Ag^+. (**A**) Schematic illustration of the fabrication of the RNA-3Ag⁺–APLNE sensing interface. Two complementary RNA strands containing three C–C mismatches were immobilized on the APLNE surface, followed by Ag⁺ intercalation into the mismatch sites. (**B**) Quantitative analysis of surface roughness (RMS roughness) before and after probe immobilization on APLNE, confirming a decrease in roughness due to the formation of the RNA-Ag⁺ molecular layer ($n = 3$). (**C**) CV curves of the RNA-Ag⁺ probe immobilized APLNE, RNA probe–APLNE, and APLNE for confirmation of Ag^+ signal in C–C mismatches of RNA probe. (**D**) Schematic comparison of probe immobilization on a conventional flat Au electrode and the APLNE, illustrating higher probe density on the nanoporous surface. (**E**) CV curves comparing the electrochemical responses of the RNA-Ag⁺ probe immobilized on the flat Au electrode and on the APLNE. (**F**) Bar graph summarizing the reduction peak currents of RNA-Ag^+–Au vs. –APLNE ($n = 3$). (**G**) Schematic illustration of RNA probes containing either one or three C–C mismatches, designed to increase the number of Ag⁺ binding sites effect on enhance signal strength. (**H**) CV curves comparing the electrochemical signals of RNA-Ag⁺ probes with one vs. three C–C mismatches immobilized on APLNE. (**I**) Bar graph summarizing the reduction peak currents of one vs. three C–C mismatches immobilized on APLNE ($n = 3$). Data represent mean ± SD for independent experiments. ***$p < 0.001$, Student's unpaired *t*-test

effective surface area of the APLNE, a higher density of RNA probes was expected to immobilize, leading to increased Ag⁺ intercalation and stronger signal output. To confirm this, electrochemical measurements using CV were performed for both electrodes under identical conditions (Fig. 3E). The RNA-3Ag⁺–APLNE electrode exhibited a much stronger redox signal compared to the RNA-Ag⁺–Au electrode, as evidenced by the pronounced increase in reduction current. This enhancement was attributed to the higher probe loading capacity and improved electron transfer kinetics enabled by the nanostructured surface of the APLNE. Quantitative comparison of CV reduction peak currents further confirmed the superior performance of the APLNE-based platform (Fig. 3F). While the RNA-3Ag⁺–Au electrode produced a modest peak current of approximately – 78.99 μA, the RNA-3Ag⁺–APLNE electrode generated a substantially stronger signal of approximately – 513.5 μA. This ~ 6.5-fold increase in signal intensity highlights the critical role of nanoscale surface engineering in maximizing the sensitivity of the electrochemical biosensor. Similarly, Lee et al. recently reported that a gold electrode on indium tin oxide with a nanoarray (GELITION), functionalized with C–C mismatched RNA-Ag⁺ probes, exhibited enhanced electrochemical responses compared to a bare Au electrode [27]. By increasing the surface area through

nanopatterning, the electrochemical signal increased from 0.8 μA to 3 μA (~ 3.8-fold). In comparison, our APLNE electrode, also functionalized with an RNA-Ag^+ probe, achieved a peak current of – 513.5 μA, representing a ~ 6.5-fold increase over the bare Au electrode. This remarkable enhancement is attributed to the highly nanoporous structure of the APLNE, which provides a substantially enlarged electroactive surface area and facilitates efficient probe immobilization. To examine the stability of the Ag^+–RNA coordination, the electrochemical responses of the RNA–Ag^+.

probes were evaluated under varying pH and temperature conditions. As a result, the reduction peak currents remained stable across physiologically relevant pH values (6.4–8.4) (Fig. S1 A, B). In addition, the electrochemical signals were also well preserved from room temperature up to 50 °C, with only moderate attenuation observed at 60 °C (Fig. S1 C, D). These results indicate that the Ag^+–RNA coordination exhibits sufficient stability against environmental fluctuations, supporting its applicability in biological sensing conditions. Collectively, these results demonstrate that the porous architecture of the APLNE provides a highly favorable interface for probe immobilization and signal amplification, a critical advantage for detecting low-abundance nucleic acid targets, particularly in amplification-free diagnostic systems.

To investigate the redox signal output of the RNA-Ag^+ sensing interface, we examined the effect of increasing the number of C–C mismatches within the RNA duplex. Unlike previous studies that typically incorporate a single C–C mismatch for Ag^+ intercalation, we designed a modified RNA probe containing three C–C mismatch sites, hypothesizing that it would allow binding of additional Ag^+ ions and thereby amplify the electrochemical signal. A schematic representation of the experimental design is shown in Fig. 3G. Two types of RNA-Ag^+ probes, one with a single C–C mismatch and the other with three mismatches, were immobilized onto APLNE substrates, and their electrochemical performance was compared under identical conditions. As shown in the CV results (Fig. 3H), the APLNE modified with the triple-mismatch probe exhibited a substantially higher reduction current than its single-mismatch counterpart. This signal enhancement is attributed to the increased number of Ag^+ coordination sites provided by the additional mismatches, allowing greater charge accumulation and transfer during the redox reaction. Quantitative analysis of the reduction peak currents (Fig. 3I) revealed a marked improvement: the electrode modified with the single C–C mismatch probe produced a peak current of approximately – 215.8 μA, whereas the triple C–C mismatched probe generated a significantly stronger current of – 513.5 μA. This ~ 2.38-fold increase confirms that rational probe design, particularly the incorporation of multiple Ag^+ binding sites, can effectively enhance the electrochemical signal without compromising the structural stability of the probe. These results validate multisite Ag^+ coordination as a practical and tunable strategy for signal amplification in electrochemical biosensing systems. Also, as shown in Supplementary Table S1, a simplified cost analysis reveals that the proposed system requires only 30 nmol of Ag^+ per assay, corresponding to a redox reporter cost (~ 0.00002 USD per test), which is substantially lower than that of conventional redox-labeled electrochemical sensors based on synthetically modified probes. By replacing expensive synthetic redox labels with inexpensive Ag^+ ions, the system improves cost-effectiveness and scalability, thereby supporting its feasibility for large-scale and practical applications.

The incorporation of C-C mismatch sites in our probe duplex was motivated by previous studies demonstrating that Ag ion can selectively coordinate with cytosine–cytosine mismatches to form a C–Ag^+–C metallo–base pair, thereby stabilizing nucleic acid duplexes both structurally and thermodynamically [28–30]. Based on this established coordination motif, we investigated whether increasing the number of C-C mismatch sites could enhance Ag^+-mediated coordination and consequently amplify electrochemical signal modulation. Although this design was sufficient to validate Ag^+-assisted duplex stabilization and Cas13a-mediated signal suppression, positional optimization of mismatch sites may further improve coordination efficiency and signal contrast, which will be explored in future work.

CRISPR/Cas13a-based amplification-free electrochemical sensing of KRAS G12D RNA using the RNA-3Ag^+–APLNE biosensor

To evaluate the functional performance of the RNA-3Ag^+–APLNE biosensor in detecting clinically relevant RNA targets, we implemented a CRISPR/Cas13a-mediated sensing strategy specifically targeting KRAS G12D ctRNA, a well-known oncogenic biomarker associated with pancreatic cancer. The operational principle of the system is schematically illustrated in Fig. 4A. In the presence of the target RNA, the CRISPR/Cas13a enzyme, guided by its corresponding CRISPR RNA (crRNA), specifically binds to the target sequence. Upon recognition, Cas13a is activated and initiates trans-cleavage activity, indiscriminately cutting surrounding single-stranded RNA, including the surface-immobilized RNA-Ag^+ probes. This enzymatic cleavage disrupts the C–C mismatched regions required for Ag^+ coordination, thereby eliminating the redox-active sites and resulting in a sharp decrease in the electrochemical signal. In contrast, when a non-target RNA sequence (5'-UUA AUG CUA AUC CUG AUA GGG GUU-3') was introduced, Cas13a remained inactive, and the RNA-Ag^+ structure stayed

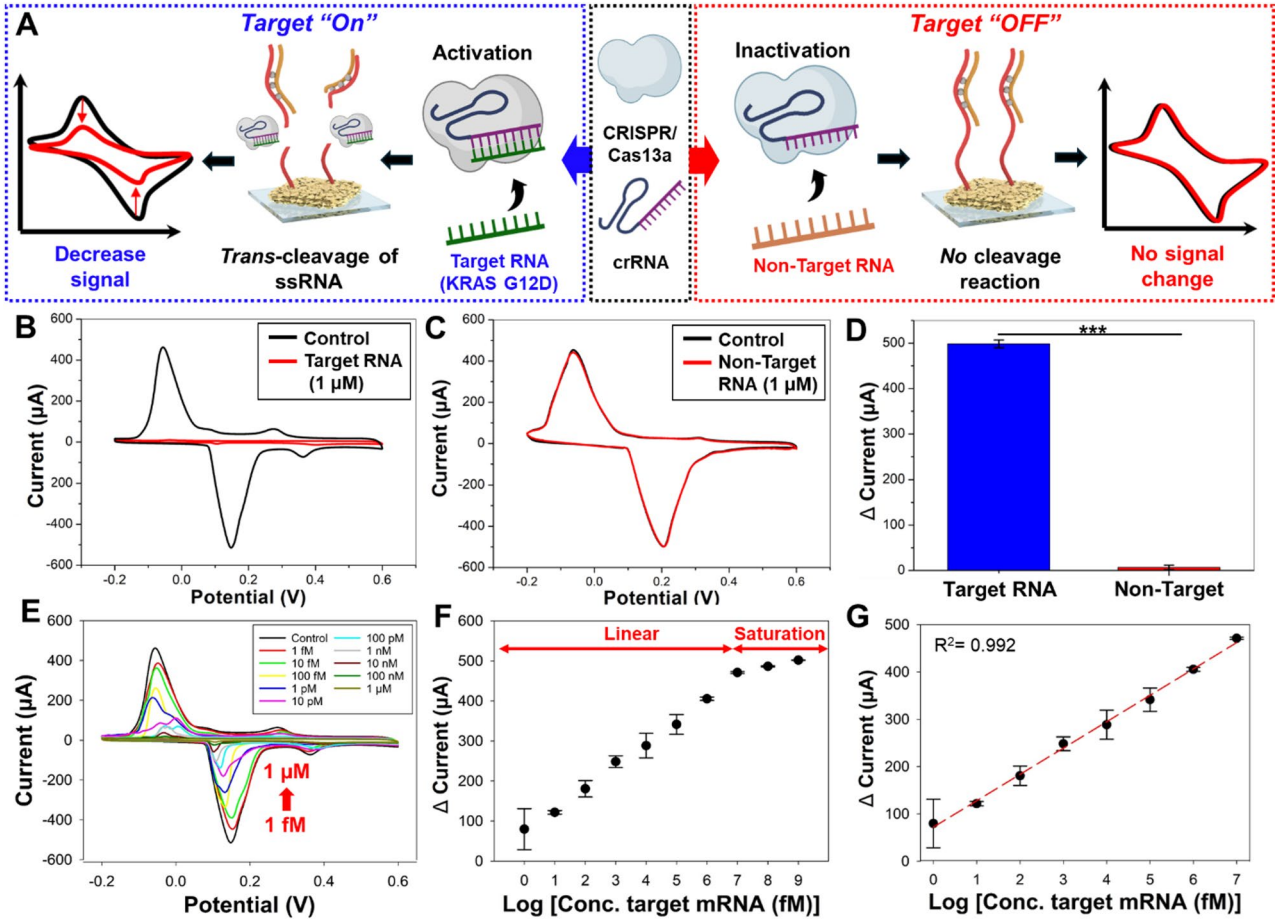

Fig. 4 CRISPR/Cas13a-based detection of KRAS G12D ctRNA using the RNA-3Ag⁺–APLNE biosensor. (**A**) Schematic illustration of the CRISPR/Cas13a detection mechanism. In the presence of target KRAS G12D RNA, activated Cas13a cleaves the surface-bound RNA-Ag⁺ probes, leading to signal suppression. In contrast, non-target RNA fails to activate Cas13a, preserving the electrochemical signal. (**B**) CV curves showing a significant decrease in the reduction current after treatment with target KRAS G12D RNA compared to the untreated control. (**C**) CV curves showing negligible signal change upon addition of non-target RNA, confirming the high sequence specificity of the biosensor. (**D**) Quantitative analysis of current differences ($\Delta Current = C - C_0$) for target and non-target RNA samples, demonstrating selective signal suppression only in the presence of the correct target ($n = 3$). (**E**) CV curves obtained at varying concentrations of target KRAS G12D RNA, showing a concentration-dependent decrease in reduction current. (**F**) Calibration curve plotting ΔCurrent against the concentration of target RNA, revealing a dynamic range up to 10 nM before saturation ($n = 3$). (**G**) Linear regression analysis of the calibration curve within the 0.01–10 nM range, yielding a high correlation coefficient ($R^2 = 0.992$) and confirming the quantitative capability of the biosensor ($n = 3$). ***$p < 0.001$, Student's unpaired *t*-test

intact, preserving the original redox current. Additional confirmation of Cas13a-mediated collateral cleavage of the surface-bound RNA probe was obtained using polyacrylamide gel electrophoresis (PAGE) (Fig. S2). In this experiment, the RNA probe showed clear band when the target RNA was absent, indicating that Cas13a was inactive under these conditions. In contrast, when the target RNA was present, Cas13a was specifically activated and induced collateral cleavage of the surface-bound RNA probe, resulting in clear degradation of the RNA which was similar with RNase treatment. These results directly confirm that the observed signal change originates from target-dependent Cas13a activity rather than nonspecific RNA degradation. In addition, the time-dependent behavior of the Cas13a-mediated electrochemical signal was examined to assess the total assay time (Fig. S3). As the reaction time increases from 5 to 20 min, the electrochemical signal change (ΔCurrent) gradually increases, reflecting ongoing RNA cleavage on the electrode surface. The signal approaches a stable level after approximately 15–20 min, indicating that the Cas13a reaction and the subsequent electrochemical signal transduction are essentially complete within this period. This result supports that the entire detection process can be reliably completed within 20 min.

To experimentally validate this detection mechanism, CV measurements were performed. As shown in Fig. 4B, application of the target KRAS G12D RNA (1 μM) to the RNA-3Ag⁺–APLNE platform resulted in a substantial reduction in current compared to the untreated control,

indicating efficient cleavage of the reporter probes and disruption of the Ag^+-coordinated redox structure. This result confirms the sensor's ability to produce a clear electrochemical signal shift in response to Cas13a activation. To assess specificity, a non-target RNA sequence (mismatched relative to the crRNA guide) was introduced under identical conditions. As shown in Fig. 4C, no notable change in the CV signal was observed, demonstrating that Cas13a remained inactive in the absence of its exact target sequence. This high sequence-specific behavior highlights the inherent strength of CRISPR-based biosensing platforms for discriminating single-nucleotide differences or mutations, an important advantage for mutation-specific diagnostics. The sequence specificity of the proposed biosensor was further evaluated by comparing the electrochemical responses to different KRAS single-nucleotide variants, including G12D, G12C, and G12V, measured under identical experimental conditions (Fig. S4). In this comparison, the sensor produces a clearly larger electrochemical signal change (ΔCurrent) for the perfectly matched KRAS G12D target, whereas only minimal signal changes are observed for the mismatched G12C and G12V sequences. This distinct difference in signal response demonstrates that Cas13a activation in the proposed system is highly sensitive to single-nucleotide differences in the target RNA, enabling robust discrimination of closely related KRAS variants.

Quantitative analysis of the reduction peak currents from CV curves is shown in Fig. 4D, where the current difference ($\Delta Current = C_0 - C$; C: current with specific target concentration, C_0: current without target) represents the signal change before and after target addition. The target RNA induced a significant ΔCurrent of approximately 498.5 μA, whereas the non-target sample produced a negligible shift (6.691 μA), further confirming both the sensitivity and specificity of the platform. To evaluate the dynamic response and detection range of the biosensor, the system was exposed to a series of KRAS G12D RNA concentrations ranging from 1 fM to 1 μM (Fig. 4E). As the target RNA concentration increased, the extent of Cas13a-mediated probe cleavage also increased, resulting in progressively suppressed redox signals. This inverse relationship between target concentration and electrochemical current forms the basis for quantitative detection. The corresponding calibration curve (Fig. 4F) was constructed by plotting ΔCurrent against target RNA concentration. The signal increased linearly from 1 fM to 10 nM, beyond which the response began to plateau. This saturation at higher concentrations is likely due to the limited availability of intact probe molecules on the electrode surface. Once most probes were cleaved, additional target RNA no longer produced further signal change. Such behavior is typical of enzymatic sensor systems, where substrate availability becomes the limiting factor at high analyte concentrations.

To determine the linear detection range more precisely, the response data from 1 fM to 10 nM were extracted and fitted to a linear regression model (Fig. 4G). The resulting curve demonstrated excellent linearity with an R^2 value of 0.992, confirming the high quantifiability of the system within this range. Based on a signal-to-noise ratio ($S/N \geq 3$) and the calibration equation $y = 55.7 \cdot \log[\text{concentration of target (fM)}] + 72.1$, the limit of detection (LOD) was calculated to be as low as 0.5 fM. Collectively, these findings demonstrate that the CRISPR/Cas13a-based RNA-3Ag^+–APLNE biosensor enables highly sensitive and specific detection of KRAS G12D RNA in an amplification-free manner. Table 1

Table 1 Comparative analysis of previously reported methods and our approach for KRAS G12D nucleic acid detection

Biosensor	Target	Method	Amplification	Time	Detection range	LOD	Ref
CRISPR/Cas9 mediated triple signal amplification platform	DNA	Optical	O	150 min	1 fM – 100 pM	0.2 fM	[31]
Nuclease-resistant DNA nanostructure composed of a single molecular beacon	DNA	Optical	O	80 min	50 fM – 160 nM	50 fM	[32]
Hybridization chain reaction-powered lab-on-fiber device	DNA	Optical	O	6 min	1.0 nM – 500 nM	0.35 nM	[33]
DNA nanoarchitecture	DNA	Optical	X	120 min	1 fM – 100 nM	0.52 fM	[34]
Screen printed carbon electrodes (SPCE)	DNA	Electrochemical	O	270 min	Few nM – few μM	-	[35]
DNAzyme/HCR sensor	DNA	Electrochemical	O	300 min	0.5 fM – 50 nM	0.5 fM	[36]
AuNP/MXene/DNA	DNA	Electrochemical	O	30 min	10 fM – 10 nM	0.38 fM	[37]
Anchor-like DNA electrochemical sensor	DNA	Electrochemical	X	90 min	0.1 pM – 10 nM	0.1 pM	[38]
CRISPR/Cas13a-based RNA-3Ag^+–APLNE	**RNA**	**Electrochemical**	**X**	**20 min**	**1 fM – 10 nM**	**0.5 fM**	**This study**

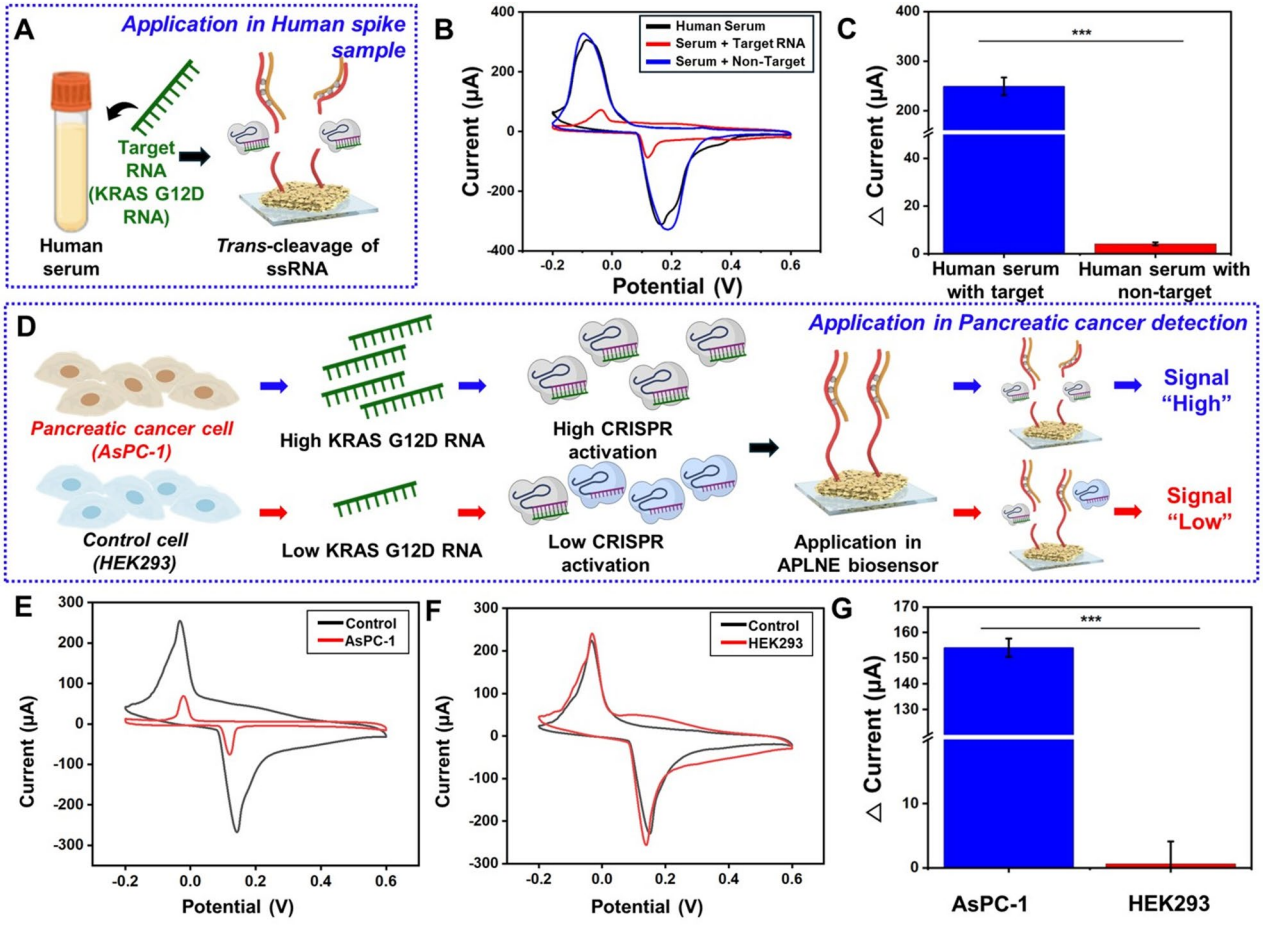

Fig. 5 (**A**) Schematic illustration of CRISPR/Cas13a-based detection of target KRAS G12D RNA in human serum using the RNA-3Ag⁺–APLNE biosensor. (**B**) CV curves of the biosensor in human serum alone, serum with target RNA (1 pM), and serum with non-target RNA (1 pM), showing selective signal suppression only in the presence of the correct target. (**C**) Quantitative analysis of current differences (ΔCurrent = C – C_0) for target and non-target RNA samples in human serum, confirming the sensor's sequence specificity under physiologically relevant conditions ($n = 3$). (**D**) Schematic illustration of CRISPR/Cas13a-mediated detection of KRAS G12D RNA in culture media from pancreatic cancer cells (AsPC-1) and healthy control cells (HEK293) using the RNA-Ag⁺–APLNE platform. (**E**) CV curves comparing responses of the RNA-Ag⁺–APLNE in culture media, and media collected from AsPC-1 cells, demonstrating signal suppression due to the presence of target RNA. (**F**) CV curves of the biosensor in culture media and media collected from HEK293 culture media, showing minimal signal change in the absence of target RNA. (**G**) Quantitative analysis of current differences (ΔCurrent = C – C_0) for biosensor responses to AsPC-1 and HEK293 culture media, demonstrating the applicability of the system for cancer-specific RNA detection in complex biological samples ($n = 3$). Data represent mean ± SD for independent experiments. ***$p < 0.001$, Student's unpaired *t*-test

summarizes the KRAS G12D electrochemical analysis performance of the biosensor. Comparison with previous studies confirms that the sensitivity and analysis time of this platform are comparable to or better than those reported in the literature.

Application of RNA-3Ag⁺–APLNE in biological samples for KRAS G12D ctRNA detection

To evaluate the practical applicability of the CRISPR/Cas13a–based RNA-3Ag⁺–APLNE biosensor in clinically relevant environments, we first tested its performance in human serum. As illustrated in Fig. 5A, human serum samples were prepared by spiking 1 pM of target RNA (KRAS G12D RNA) or 1 pM of non-target RNA, and these samples were applied to the biosensor. As illustrated in Fig. 5B, CV analysis revealed a clear decrease in redox current peak upon introduction of KRAS G12D target RNA compared to the blank serum sample, whereas no significant signal change was observed with non-target RNA under identical conditions. This result demonstrates the biosensor's high specificity in complex biological matrices. Quantitative analysis of the current differences (ΔCurrent, ΔC = C – C_0) is shown in Fig. 5C. A substantial decrease in current was observed in the target RNA group (ΔC_{target} = 248.92 μA), while the non-target group showed minimal variation ($\Delta C_{non-target}$ = 4.06 μA), confirming the system's specificity and resistance to nonspecific activation in serum.

To further validate the biosensor's ability to detect endogenously expressed cancer-associated RNA, we applied it to cell culture media derived from both cancerous and healthy cell lines. As illustrated in Fig. 5D, media were collected from the pancreatic cancer cell line AsPC-1, which overexpresses KRAS G12D ctRNA, and from the healthy control cell line HEK293, which expresses low levels of the target RNA. These samples were then introduced into the CRISPR/Cas13a-based biosensor and analyzed. As shown in Fig. 5E, the biosensor exposed to AsPC-1 media exhibited a strong decrease in redox current compared to the blank medium. In contrast, the biosensor applied to HEK293 media (Fig. 5F) showed no appreciable signal suppression, consistent with the absence of the KRAS G12D mutation in this healthy cell line.

A quantitative comparison of the electrochemical signal changes (ΔCurrent) further demonstrates the ability of the biosensor to distinguish between cancer-derived and healthy cell culture media. As shown in Fig. 5G, a pronounced signal change is observed for AsPC-1 cancer cell media (ΔC_{AsPC-1} = 154.10 μA), whereas only a negligible signal change is detected for HEK293 control media (ΔC_{HEK293}= 0.60 μA), even in complex biological fluids such as culture supernatants. To further validate the quantitative reliability of the electrochemical readout, KRAS G12D RNA levels in AsPC-1 culture media were independently quantified by qRT-PCR and compared with the values obtained from the electrochemical biosensor (Fig. S5). The relative KRAS G12D RNA levels measured by qRT-PCR exhibit strong agreement with the results from the biosensor. Notably, the KRAS G12D RNA concentration determined by the electrochemical sensor (6.25 pM) closely matches the value quantified by qRT-PCR (6.65 pM). These results indicate that the electrochemical signal change reliably reflects the abundance of KRAS G12D RNA in cell culture media, supporting both the quantitative reliability and biological relevance of the proposed biosensing platform.

Collectively, these results demonstrate that the RNA-$3Ag^+$–APLNE biosensor based on the CRISPR/Cas13a system enables sensitive and selective detection of cancer-associated RNA biomarkers not only in buffer but also in clinically relevant matrices such as serum and cell culture media. The platform maintains robust specificity, signal stability, and efficient electrochemical transduction even in complex biological environments, supporting its potential for future clinical diagnostic applications, including liquid biopsy and point-of-care cancer detection. In addition, the versatility of the biosensing architecture was demonstrated by targeting an independent RNA sequence, SARS-CoV-2 RNA, through simple redesign of the corresponding crRNA and RNA probe (Fig. S6). Under these conditions, a clear decrease in reduction peak current was observed only in the presence of the SARS-CoV-2 target, while no significant signal change was detected in the control sample. This result confirms that the proposed platform can be readily adapted to different RNA targets by modifying the CRISPR guide and probe design, without altering the electrode structure or the underlying detection principle.

Conclusions

In this study, we developed a novel amplification-free electrochemical biosensor by integrating a CRISPR/Cas13a-based RNA recognition mechanism with an RNA-$3Ag^+$ probe and APLNE. The combination of a highly structured APLNE and a triple C–C mismatched RNA duplex enabled dense probe immobilization and multi-site Ag^+ coordination, resulting in greatly amplified electrochemical signals without the need for target amplification or synthetic redox reporters. Using this integrated system, our biosensor demonstrated excellent analytical performance for detecting KRAS G12D ctRNA, achieving a detection limit of 0.5 fM and a linear dynamic range from 1 fM to 10 nM within 20 min. Notably, the platform exhibited high specificity in complex biological samples, including human serum and pancreatic cancer cell culture media, validating its robustness under physiologically relevant conditions. By eliminating multi-step nucleic acid amplification workflows and avoiding toxic labeling reagents, the biosensor provides a simple, cost-effective, and environmentally friendly solution for RNA detection. Beyond its strong analytical performance, the platform offers exceptional potential for clinical translation due to its modular design, which can be easily adapted to detect virtually any RNA target by modifying the CRISPR guide sequence and probe. This adaptability supports not only multiplexed detection of diverse ctRNA biomarkers in oncology but also broader applications in RNA-based diagnostics for infectious diseases, genetic disorders, and real-time monitoring of therapeutic responses. By combining high sensitivity, rapid turnaround, and broad target compatibility, this biosensor represents a promising tool for next-generation point-of-care diagnostics and personalized medicine.

Experimental section

Materials

Glass substrates coated with indium tin oxide (ITO) (surface resistance: 15 Ω/cm^2, thickness: 0.7 mm, active patterning area: 1.2 × 1.2 cm^2) were obtained from the National Nanofab Center (South Korea). Reagents, including potassium hexacyanoferrate(II) trihydrate, potassium hexacyanoferrate(III), Triton X-100, and silver nitrate ($AgNO_3$) were purchased from Sigma-Aldrich (USA). Gold and silver-plating solutions were obtained from Thermo Fisher Scientific (Waltham, MA,

USA). Photoresist-related materials, including AZ EBR solvent, UV-cross-linkable photoresist (AZ2020), and AZ 300 MIF developer, were supplied by Merck KGaA (Darmstadt, Germany). Dimethyl sulfoxide (DMSO) was obtained from Corning (Corning, NY, USA). Polydimethylsiloxane (PDMS) components, including Sylgard 184 silicone elastomer base and curing agent, were purchased from Dowhitech (Seongnam, South Korea). For RNA experiments, a variety of single-stranded RNAs (ssRNAs) were employed, including thiolated probe-1 (Thiolated-5'-AUG GCA UGG CAU GGC GGG GCG GG-3'), probe-2 (5'-CCC CCC CCC CCU G C-3'), and a CRISPR guide RNA (crRNA, 5'-GAU UUA GAC UAC CCC AAA AAC GAA GGG GA CUA AAA CUC UGC UCC AAC UAC CAC AAG U-3'), which specifically targets the KRAS G12D mutation (5'-ACU UGU GGU AGU UGG AGC AGA-3').

Coating and patterning of ITO substrates

ITO substrates were sequentially cleaned by sonication in 1% Triton X-100, ethanol, and deionized water (DW) for 10 min each. A photoresist (PR) solution was prepared by mixing stock PR and PR solvent in a 6:4 ratio, and 20 μL of this mixture was spin-coated onto a cleaned ITO substrate at 4,000 rpm for 20 s using a spin coater (Laurell Technologies, USA). The PR-coated substrate was pre-baked on a hot plate at 100 °C for 60 s. Ultraviolet (UV) exposure was performed using a He-Cd laser (Kimmon Koha Laser Systems, Japan) with a wavelength of 1,000 nm and an intensity of 0.5 mW. A Lloyd's mirror interferometer was employed to generate a periodic interference pattern through the superposition of direct and reflected light, producing a uniform PR pattern. Based on prior studies, an incidence angle of 144.35° was applied to achieve a PR grating pattern with a 1,000 nm pitch. To fabricate dot-shaped PR patterns, the substrate was exposed to UV light, rotated 90°, and subjected to a second 10 s UV exposure. After dual exposure, the substrate was post-baked at 110 °C for 1 min to promote cross-linking of the exposed PR regions. Unexposed PR was removed by immersing the substrate in a developer solution for 20 s, forming a well-defined dot array with a feature size of approximately 500 nm. All fabrication steps were performed under controlled environmental conditions (ambient temperature < 20 °C, relative humidity < 40%) to ensure pattern fidelity and reproducibility.

Fabrication of APLNE

To fabricate the APLNE, a 3D-printed hole chamber was attached to the PR-patterned ITO substrate using PDMS as an adhesive and sealing material. Electrochemical deposition was carried out in a conventional three-electrode setup, with a platinum wire as the counter electrode, a silver/silver chloride (Ag/AgCl) double-junction electrode as the reference electrode, and the PR-patterned substrate as the working electrode. Gold electrodeposition was performed using a multipotential step method on a CHI 600E electrochemical workstation (CH Instruments, Inc., TX, USA) with the following parameters: applied potential – 0.95 V, sampling interval 0.032 s, resting time 2 s, and sensitivity 1.0×10^{-3} A/V. The deposition lasted 45 s, forming a metallic Au base layer. Subsequently, a mixed Au/Ag solution (6:1 ratio) was electrodeposited under the same conditions for 10 s. After deposition, the PR pattern was removed using DMSO, and the silver component was selectively etched using nitric acid to yield a porous gold nanostructure. The resulting APLNE was stored in ethanol for subsequent experiments.

Characterization of APLNE

The surface morphology of the fabricated dot PR pattern, planar Au/Ag lattice, and APLNE was characterized using atomic force microscopy (AFM, NX-10, Complete Systems, South Korea) and field-emission scanning electron microscopy (FE-SEM, JSM-7100 F, Japan). For SEM imaging of the PR pattern, a 20 nm-thick Au conductive layer was deposited by sputtering using a metal ion sputter coater (KIC-1 A, COXEM, South Korea). AFM measurements were performed in non-contact mode with a scan rate of 0.5 Hz and a resonant frequency of 330.99 kHz. The Z servo gain was set to 1.2, and imaging was conducted over a 1 μm × 1 μm area (X and Y directions) with a resolution of 256 × 256 pixels. The Z height was adjusted to maintain stable tip–sample interaction. Height profile analysis was performed using XEI software. To evaluate the redox signal enhancement capability of APLNE, CV was conducted using a CHI 600E potentiostat (CH Instruments, Inc., TX, USA) in an electrolyte solution containing 10 mM ferricyanide $[Fe(CN)_6]^{3-}$. Measurements were performed for APLNE, Au lattice nanoelectrodes, and bare ITO substrates under identical conditions.

Fabrication of RNA-3Ag$^+$–APLNE biosensor

The APLNE substrate was first rinsed with DW and incubated with 30 μL of 10 μM thiolated RNA probe-1 at 4 °C for 3 h. Subsequently, 30 μL of a modified version of RNA probe-1, referred to as sensing probe-2, was immobilized on the APLNE at 4 °C for 1 h to form a double-stranded RNA duplex containing three C–C mismatches. After duplex formation, 30 μL of 1 mM $AgNO_3$ solution was applied to the substrate, allowing Ag^+ ions to selectively coordinate with the mismatched C–C sites. The metallization reaction was carried out at 4 °C for 1 h, resulting in the formation of a mismatched RNA-Ag^+ nanocomposite on the APLNE surface. After each immobilization

step, the electrode was thoroughly rinsed with DW and dried under N_2 gas.

Electrochemical detection of KRAS G12D RNA using a CRISPR/Cas13a-based RNA-3Ag$^+$– APLNE biosensor

The RNA-3Ag$^+$–APLNE biosensor was prepared as described above. Target RNA concentrations ranging from 1 μM to 1 fM were tested to evaluate sensor sensitivity. To assess the biosensing capabilities of the prepared CRISPR/Cas13a, target RNA, Cas13a (10 nM), and crRNA (10 nM) were mixed in a 1:1:1 ratio to a final volume of 30 μL and incubated at 24 °C for 20 min to activate the CRISPR/Cas13a system. Following incubation, the electrode was rinsed with DW to remove the reaction mixture. Electrochemical measurements were conducted via CV analysis in Dulbecco's phosphate-buffered saline (DPBS) as the electrolyte, using a three-electrode setup consisting of a platinum wire counter electrode, a double-junction Ag/AgCl reference electrode, and the RNA-Ag$^+$–functionalized APLNE working electrode. Redox signals of Ag$^+$ ions inserted into the C–C mismatched sequences were recorded under the following conditions: potential range – 0.1 to 0.6 V, resting time 2 s, sampling interval 0.001 V, scan rate 0.05 V/s, and sensitivity 1.0×10^{-5} A/V. To evaluate stability, the biosensor was stored at 4 °C and analyzed weekly via CV.

AsPC-1 and HEK293 cell culture and conditioned medium collection

AsPC-1 and HEK293 cells were obtained from the Korea Cell Line Bank (KCLB, Seoul, Korea) and maintained in Dulbecco's Modified Eagle Medium (DMEM) supplemented with 100 U/mL penicillin, 100 mg/mL streptomycin (Welgene, Gyeongsan, Korea), and 10% fetal bovine serum (Welgene) at 37 °C in a humidified incubator with 5% CO_2. Cells were seeded at a density of 2×10^5 cells/well, and conditioned medium was collected after 24 h for subsequent biosensor testing.

Supplementary Information

The online version contains supplementary material available at https://doi.org/10.1186/s13036-026-00641-0.

Supplementary Material 1

Acknowledgements
Not applicable.

Author contributions
Y.-R. Lee: Writing – original draft, Writing – review & editing, Methodology, Investigation, Formal analysis, Data curation. M.-J. Lee: Writing – original draft, Writing – review & editing, Methodology, Formal analysis, Data curation. S.-N. Lee: Writing – review & editing, Supervision, Funding acquisition and Project administration. J.-W. Choi: Writing – original draft, Writing – review & editing, Supervision, Resources, Conceptualization, Funding acquisition and Project administration. All authors read and approved the final manuscript.

Funding
This work was supported by the National Research Foundation of Korea(NRF) grant funded by the Korea government(MSIT)(RS-2024-00344633), by National R&D Program through the National Research Foundation of Korea(NRF) funded by Ministry of Science and ICT(NRF-2022M3H4A1A01005271(RS-2022-NR068121)), and by GRDC Cooperative Hub through the National Research Foundation of Korea funded by the Ministry of Science and ICT (Grant number RS-2023-00259341).

Data availability
Data will be made available on request.

Declarations

Ethics approval and consent to participate
Not applicable.

Consent for publication
Not applicable.

Competing interests
Author Sang-Nam Lee was employed by Uniance Gene Inc. The remaining authors declare that the research was conducted in the absence of any commercial or financial relationships that could be construed as a potential conflict of interest.

Author details
[1]Department of Integrative Bioengineering, Sogang University, Seoul 04107, Republic of Korea
[2]Department of Chemical & Biomolecular Engineering, Sogang University, 35, Baekbeom-ro, Mapo-gu, Seoul 04107, Republic of Korea
[3]Uniance Gene Inc., Seoul 08381, Republic of Korea

Received: 22 October 2025 / Accepted: 11 February 2026
Published online: 23 February 2026

References

1. Hulstaert E, Morlion A, Levanon K, Vandesompele J, Mestdagh P. Gynecol Oncol. 2021;160:633.
2. Islam MN, Masud MK, Haque MH, Al Hossain MS, Yamauchi Y, Nguyen NT, Shiddiky MJA. Small Methods. 2017;1:1700131.
3. Fleige S, Pfaffl MW. Mol Aspects Med. 2006;27:126.
4. Crunkhorn S. Nat Rev Drug Discov. 2017;16:529.
5. Hu J, Sheng Y, Kwak KJ, Shi J, Yu B, Lee LJ. Nat Commun. 2017;8:1.
6. Raez LE, Danenberg K, Sumarriva D, Usher J, Sands J, Castrellon A, et al. Cancer Drug Resist. 2021;4:1061.
7. Zou S, Zhang L, Jiang C, Li F, Yang Y, Deng X, et al. Cancer Lett. 2024;599:217134.
8. López-Palacios A, Aranda MN, Caballos I, Hernández-Montoto A, Calabuig E, Gómez-Ruiz MD, et al. Sens Actuators Rep. 2025;9:100298.
9. Zakiyyah SN, Irkham, Sima KSP, Kharismasari CY, Xi M, Gaffar S, et al. Sens Actuators Rep. 2025;10:100358.
10. Makarova KS, Haft DH, Barrangou R, Brouns SJJ, Charpentier E, Horvath P, et al. Nat Rev Microbiol. 2011;9:467.
11. Choi JH, Yoon J, Chen M, Shin M, Goldston LL, Lee KB, Choi JW. Biochip J. 2025;19:167.
12. Yang H, Patel DJ. Nat Chem Biol. 2024;20:673.
13. Liu L, Li X, Ma J, Li Z, You L, Wang J, et al. Cell. 2017;170:714.
14. Zhou J, Yin L, Dong Y, Peng L, Liu G, Man S, Ma L. Anal Chim Acta. 2020;1127:225.
15. Sheng Y, Zhang T, Zhang S, Johnston M, Zheng X, Shan Y, et al. Biosens Bioelectron. 2021;178:113027.
16. El-Said WA, Al-Bogami AS, Alshitari W, El-Hady DA, Saleh TS, El-Mokhtar MA, Choi JW. Biochip J. 2021;15:287.
17. Shanbhag MM, Manasa G, Mascarenhas RJ, Mondal K, Shetti NP. Chem Eng J Adv. 2023;16:100516.
18. Zhu C, Yang G, Li H, Du D, Lin Y. Anal Chem. 2015;87:230.
19. Ren T, Bramlitt SE, LaFreniere JMJ, Seitz WR, Halpern JM. Sens Actuators Rep. 2021;3:100066.

20. Muzammal S, Ahmad A, Sheraz M, Kim J, Ali S, Hanif MB, et al. Energy Convers Manage:X. 2024;22:100547.
21. Yu F, Tian F, Zou H, Ye Z, Peng C, Huang J, et al. J Hazard Mater. 2021;415:125511.
22. Li L, Liu W, Dong H, Gui Q, Hu Z, Li Y, et al. Adv Mater. 2021;33:2004959.
23. Huang R, Du H, Cheng L, Zhang P, Meng F, Zhong Z. Acta Biomater. 2023;168:529.
24. McIntyre CA, Grimont A, Park J, Meng Y, Sisso WJ, Seier K, et al. Cancer Cell. 2024;42:1614.
25. Pane K, Zanfardino M, Grimaldi AM, Leone I, Nuzzo S, Salvatore M, Franzese M. Cancer Med. 2025;14.
26. Mehennaoui S, Poorahong S, Jimenez GC, Siaj M. Sci Rep. 2019;9:1.
27. Lee Y, Lee JH, Lee T, Shin M, Yoon J. ACS Sens. 2025;10:4370.
28. Oliveira LM, Long AS, Brown T, Fox KR, Weber G. Chem Sci. 2020;11:8273–87.
29. Ono A, Cao S, Togashi H, Tashiro M, Fujimoto T, Machinami T, Oda S, Miyake Y, Okamoto I, Tanaka Y. Chem Commun. 2008;39:4825.
30. Torigoe H, Okamoto I, Dairaku T, Tanaka Y, Ono A, Kozasa T. Biochimie. 2012;94(11):2431.
31. Zhou M, Wang H, Li C, Yan C, Qin P, Huang L. Anal Chim Acta. 2022;1230.
32. Xue C, Wang L, Huang H, Wang R, Yuan P, Wu ZS. ACS Sens. 2021;6:4029.
33. Xu J, Han X, Xu W, Liu J, Zhu A, Song D, Long F. Talanta. 2023;259.
34. Xue G, Huang H, Hua L, Chen B, Dong H, Jia H, et al. Sens Actuators B Chem. 2024;420:136513.
35. Attoye B, Baker MJ, Thomson F, Pou C, Corrigan DK. Biosensors (Basel). 2021;11.
36. Zhou X, Liu X, Xia X, Yang X, Xiang H. J Electroanal Chem. 2020;870:114270.
37. Yu X, Bai S, Wang L. Front Bioeng Biotechnol. 2023;11:1176046.
38. Zeng N, Xiang J. Talanta. 2019;198:111.

† These authors contributed equally to this work.

Publisher's note